



香港天文台

HONG KONG OBSERVATORY

Reprint 522

Terminal Doppler Weather Radar Observation of Atmospheric  
Flow over Complex Terrain during Tropical Cyclone Passages

C.M. Shun, S.Y. Lau & O.S.M. Lee

Journal of Applied Meteorology, Volume 42, p. 1697-1710

*Permission to place a copy of this work on this server has been provided by the American Meteorological Society. The AMS does not guarantee that the copy provided here is an accurate copy of the published work.*

## Terminal Doppler Weather Radar Observation of Atmospheric Flow over Complex Terrain during Tropical Cyclone Passages

C. M. SHUN, S. Y. LAU, AND O. S. M. LEE

*Hong Kong Observatory, Hong Kong, China*

(Manuscript received 11 December 2002, in final form 25 May 2003)

### ABSTRACT

A Terminal Doppler Weather Radar (TDWR) started operation in Hong Kong, China, in 1997 for monitoring wind shear associated with thunderstorms affecting the Hong Kong International Airport. The airport was built on land reclaimed from the sea and lies to the immediate north of the mountainous Lantau Island, which has hills rising to nearly 1000 m. Since 1997, the airport experienced a number of tropical cyclone passages, some bringing strong southerly winds across these hills. Under these conditions the TDWR captured interesting but complex flow patterns in the lower atmosphere. The TDWR Doppler velocity datasets reveal features not previously observed with conventional instruments. These include shear lines, reverse flow, small-scale vortices, streaks of low-speed flow set against a high-speed background, as well as gap-related downslope high-speed flow. Hovmöller diagrams constructed from the Doppler velocity data bring out in considerable detail periodic shedding of vortices and transient wind patterns in the wake of the hills.

### 1. Introduction

The Hong Kong International Airport (HKIA) came into operation in July 1998. Immediately south of HKIA is the mountainous Lantau Island. Figure 1 shows the location of the airport and the complex terrain of Lantau Island. Lantau is oriented east-northeast–west-southwest, with a width of about 5 km and length of about 20 km. In the middle, several peaks, namely, Nei Lak Shan (NLS; 751 m MSL), Lantau Peak (LP; 934 m MSL), Sunset Peak (869 m MSL), and Lin Fa Shan (766 m MSL), form a U-shaped ridge. Saddlelike cols as low as 340–460 m MSL separate these peaks, the most prominent one being the Tung Chung Gap (340 m MSL) between Lantau Peak and Sunset Peak. To support airport operations, a Terminal Doppler Weather Radar (TDWR) system was installed in 1997 for detecting microburst and wind shear associated with thunderstorms and other weather events. Weather sensors for wind shear and turbulence alerting also include ground-based anemometers installed in and around HKIA, and their locations are indicated in Fig. 1 to facilitate the discussion below. An overview of the wind shear and turbulence-alerting facilities and new developments to improve the alerting techniques is given in Shun (2003).

To better understand the occurrence of terrain-induced wind shear and turbulence (TIWT) generated by airflow over Lantau, a study based on field measure-

ments and numerical simulations was conducted in 1994 (Neilley et al. 1995) prior to the airport opening. This study identified two sources of TIWT downwind of Lantau: (i) moderate turbulence associated with gravity wave dynamics for critical-level flow under stably stratified conditions and (ii) severe mechanical turbulence associated with deep uniform flow. It also concluded that terrain-induced wind shear was considerably less intense and less frequent as compared with terrain-induced turbulence, with peak wind shear events only marginally significant and occurring during very significant turbulence episodes. As part of this study, Clark et al. (1997) used a high-resolution numerical model to simulate a case of severe turbulence reported by a King Air research aircraft downwind of Lantau during the passage of Tropical Storm Russ on 7 June 1994. Clark et al. (1997) concluded that mechanical effects rather than gravity wave dynamics dominated the flow distortion and generation of turbulence downwind of Lantau under deep uniform flow. Aircraft pilot reports received since the opening of HKIA, however, indicate that, apart from terrain-induced turbulence, significant wind shear also occurred downwind of Lantau in both stably stratified conditions and deep uniform flow.

This paper presents interesting but complex three-dimensional atmospheric flow and terrain-induced wind shear phenomena observed by the TDWR downwind of Lantau during passages of two tropical cyclones, one in 1997 and one in 1999. Wind patterns not previously observed by conventional instruments under similar conditions, especially their spatial and temporal varia-

---

*Corresponding author address:* C. M. Shun, Hong Kong Observatory, 134A Nathan Road, Hong Kong, China.  
E-mail: cmshun@hko.gov.hk

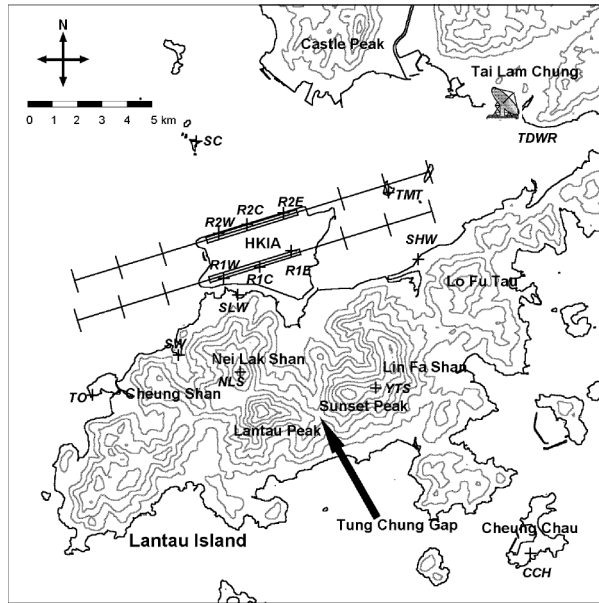


FIG. 1. Map of HKIA and its surrounding areas. Terrain contours are given in 100-m intervals. Locations of the TDWR and ground-based anemometers are indicated. The tick marks along the extended axes of the runways give the specific distance (1, 2, and 3 n mi) from the runway ends.

tions, will be highlighted. Section 2 provides background information on the use and interpretation of the TDWR data shown in the subsequent sections. Sections 3 and 4 present TDWR Doppler velocity observations captured during the passage of Typhoon Victor in 1997 and Typhoon Maggie in 1999. Although both tropical cyclones brought strong southerly flow to the Lantau area, different wind patterns were observed on these two occasions. As will be discussed, these differences were due to the highly three-dimensional complex terrain of Lantau projecting different cross sections toward the different flow directions, namely, southwesterly versus southerly. These two occasions, therefore, warrant separate discussions. Section 5 summarizes our current understanding of the observed phenomena, suggests areas to be explored further to improve this understanding, and provides conclusions to the paper.

## 2. TDWR in Hong Kong

The TDWR is strategically located at Tai Lam Chung (Fig. 1), about 12 km northeast of HKIA, to enable a clear view of the airport runways, and the approach and departure areas. Because its line-of-sight toward the airport is practically aligned with the orientation of the runways, the Doppler radial velocity thus observed provides a good estimate of the head or tail wind component and, hence, the possible wind shear experienced by landing or departing aircraft. To avoid beam blockage by nearby ships, the radar antenna of the TDWR was installed at about 60 m MSL.

The TDWR is a 250-kW peak power C-band system with a high-performance antenna with half-power beam-width of  $0.55^\circ$ . It is essentially the same system implemented by the U.S. Federal Aviation Administration (FAA) (Michelson et al. 1990) at more than 40 airports in the United States. The radar has a highly stable klystron-based amplifier that enables clutter suppression of up to 55 dB. Although the TDWR was designed to detect microbursts and wind shear associated with thunderstorms, its radar data enables detection of wind shear brought about by other mechanisms under rainy conditions. The TDWR routinely makes azimuthal scans at different elevation angles in accordance with the scan strategy in operation. The radar base data (reflectivity, Doppler radial velocity, spectrum width, and signal-to-noise ratio) have range gate spacing of 150 m and an azimuth interval of  $1^\circ$ . The lowest elevation angle employed for automatic wind shear detection is  $0.6^\circ$ . During normal operation, the “monitor mode” essentially makes continuous  $360^\circ$  azimuthal scans at different elevation angles. When the TDWR detects either wind shear or significant precipitation area, it will automatically switch to the “hazardous weather mode.” In this mode, the radar makes sector azimuthal scans confined to the airport approach and departure areas only. This enables the wind shear detection scan to be repeated at intervals of less than 1 min. For operational reasons, no RHI scans are made in these modes.

Because the TDWR has to operate in a high-clutter environment with both stationary and moving targets, sophisticated clutter-removal algorithms are used to provide quality-controlled radar base data (“conditioned data”) for automatic wind shear detection. These algorithms include the use of (i) 55-dB frequency domain filters that provide high-pass band filtering of targets with small or zero radial velocity; (ii) four different Clutter Residue Editing Maps (CREMs) for removal of residual stationary clutter at the four lowest elevation angles ( $0.6^\circ$ ,  $1.0^\circ$ ,  $2.4^\circ$ , and  $6.0^\circ$ ); (iii) clutter polygons to eliminate sidelobe contamination at  $0.6^\circ$  and  $1.0^\circ$  for the area over and south of Lantau Island, over which the main radar beam is blocked by the Lantau terrain; and (iv) point target filters that remove spikelike anomalies in radar reflectivity caused by moving objects, such as aircraft, birds, automobiles, and marine vessels. The system is also provided with velocity dealiasing [using dual scans with different pulse repetition frequencies (PRFs)], signal-to-noise thresholding, and range obscuration–editing algorithms to ensure that the Doppler radial velocity data are free from contamination. After passing through these quality-control algorithms, the conditioned data are then processed by several weather detection and warning algorithms for automatic generation of wind shear alerts and graphical products for users. The radar data presented in this paper are all conditioned data.

For presentation of TDWR data in this paper, the conditioned data from azimuthal scans in polar coord-

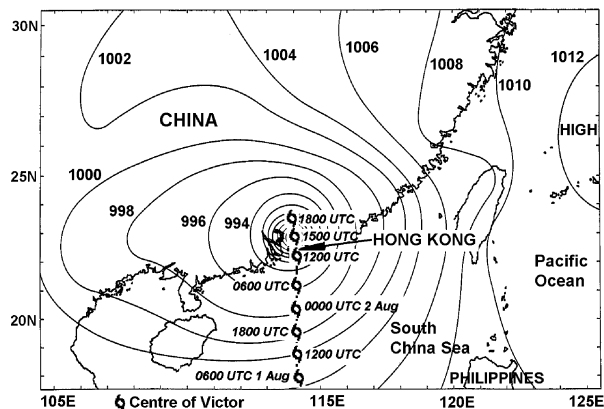


FIG. 2. Surface pressure chart at 1500 UTC 2 Aug 1997 with the track of Victor overlaid.

dinates were mapped onto a display in Cartesian coordinates with grid resolution of  $100\text{ m} \times 100\text{ m}$ . Hovmöller diagrams presented in this paper were produced by mapping and interpolating conditioned data at selected range bins and scan times onto the appropriate space–time grids. Care must be exercised when interpreting these Hovmöller diagrams, because of the discrete nature of the radar scans in both space (especially in the vertical) and time.

### 3. Typhoon Victor—First observation of velocity streaks and reverse flows

Typhoon Victor was the first tropical cyclone passing over Hong Kong since the TDWR was put into trial operation in early 1997. Victor first formed to the south of Hong Kong on 31 July 1997 and by 2 August it had intensified into a typhoon with estimated maximum winds of  $33\text{ m s}^{-1}$ . On the same day it moved north and made landfall over Hong Kong at around 1200 UTC (2000 LT,  $\text{LT} = \text{UTC} + 8\text{ h}$ ). It weakened into a severe tropical storm with estimated maximum winds of  $31\text{ m s}^{-1}$  at the same time. Its center skirted the northeastern tip of Lantau Island. Figure 2 shows the surface pressure chart at 1500 UTC with the track of Victor overlaid.

Figure 3 shows the wind and temperature profiles from the radiosonde ascent launched at 1200 and 1800 UTC at King’s Park Meteorological Station, some 25 km east of HKIA. As Victor tracked northward, low-level winds at King’s Park veered from south-southwest to southwest. Apart from the lowest 500 m over which the local wind flow might have been affected by hills within several kilometers of King’s Park, the wind speeds generally increased with height in the lowest 2000 m, ranging between 15 and  $30\text{ m s}^{-1}$ . The average Brunt–Väisälä frequency ( $N$ ) between 500 and 1500 m MSL is estimated to be about  $0.012\text{ rad s}^{-1}$ .

As Victor moved farther inland, the winds at HKIA gradually backed from northwesterly to southwesterly after 1300 UTC and became disrupted by the Lantau

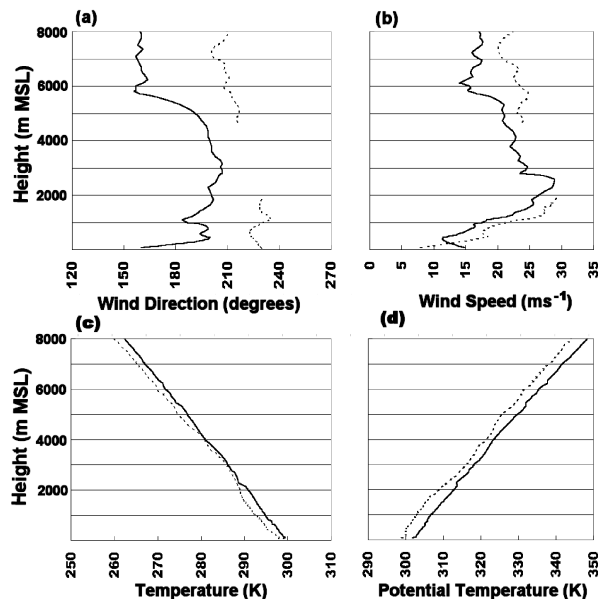


FIG. 3. King’s Park radiosonde ascent at 1200 (solid lines) and 1800 (dotted lines) UTC 2 Aug 1997: (a) wind direction ( $^{\circ}$ ), (b) wind speed ( $\text{m s}^{-1}$ ), (c) temperature (K), and (d) potential temperature (K). Note that wind data were not available between 1900 and 4500 m MSL at 1800 UTC.

terrain, especially by the U-shaped ridge in the middle. This disrupted flow in the presence of precipitation was detected by the TDWR and wind shear alerts were generated for the eastern approach area starting at 1320 UTC. Because the southwesterly flow was generally aligned with a number of radials of the TDWR, the case of Victor provided very good radial velocity data for analyzing the disrupted flow downwind of Lantau.

#### a. Radial velocity data of azimuthal scans

Figure 4a shows the TDWR radial velocity data at  $0.6^{\circ}$  elevation at 1402 UTC. Maximum radial winds of up to about  $-30\text{ m s}^{-1}$  (i.e., toward the radar or inbound) were observed over and to the east of HKIA. These agreed well with the maximum 1-min southwesterly wind gust of about  $28\text{ m s}^{-1}$  recorded by the surface anemometer at station R1E (see Fig. 1 for location) over HKIA. Greatly contrasting this were the very small inbound radial winds (i.e., in green on the velocity color scale) observed near the coast of Lantau south of HKIA. This condition persisted for several hours, until 1900 UTC when the southwesterly winds gradually weakened.

Over the strong shear region described above, streaks and bubbles of smaller inbound radial velocity were observed to emanate from the terrain of Lantau downwind of Nei Lak Shan. The width of these low (radial)-speed streaks and the size of the low-speed bubbles were on the order of several hundred meters. The radial velocities of these streaks and bubbles were typically 10

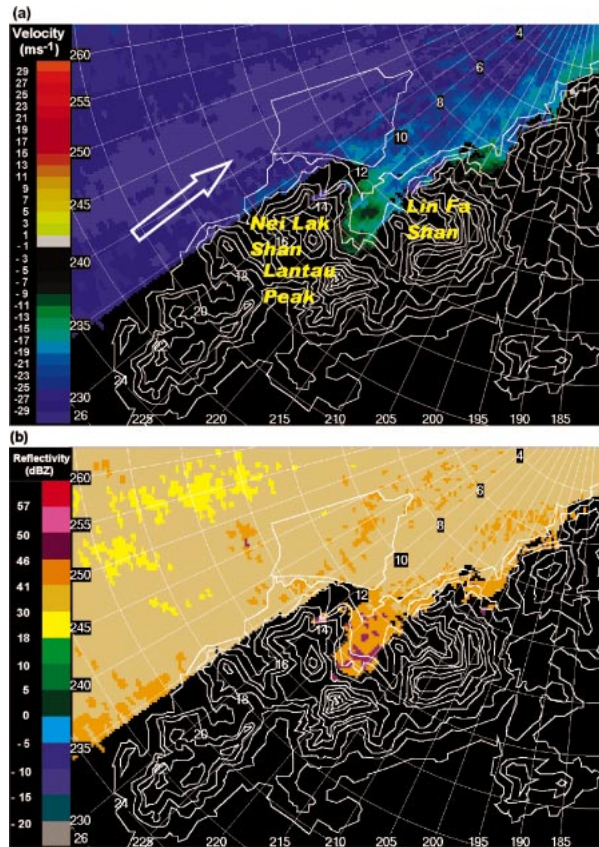


FIG. 4. (a) TDWR radial velocity display and (b) TDWR reflectivity display at  $0.6^\circ$  elevation at 1402 UTC 2 Aug 1997. Radar range rings are labeled every 2 km, and azimuths are labeled every  $5^\circ$ . White arrow in (a) indicates background flow direction.

$\text{m s}^{-1}$  less than that of the background high-speed flow. The time-dependent characteristics of these streaks and bubbles will be elicited by means of Hovmöller diagrams to be presented later in sections 3b and 3c. Figure 4b shows the reflectivity field obtained in the same scan that provided the velocity field in Fig. 4a. We note that the whole area was covered by precipitation, which appeared to be rather uniformly distributed with reflectivity mostly between 30 and 40 dBZ. This uniformly distributed precipitation pattern persisted over the next 2 h.

Similar low-speed streaks and bubbles can also be observed at  $1.0^\circ$  (Fig. 5) and  $2.4^\circ$  (Fig. 6) elevations. More interesting, in Fig. 6, small areas of positive (outbound) radial velocities (i.e., in yellow on the velocity color scale) can be seen just downwind of the individual peaks of the U-shaped ridge. Without isolated spikes of doubtful velocity data, the outbound velocities downwind of these peaks reached  $3\text{--}8 \text{ m s}^{-1}$ . While the outbound velocity area stayed rather close to the lee of Nei Lak Shan, the two other outbound velocity areas extended as far as 1.5 km downwind of Lantau Peak and Lin Fa Shan.

Inspection of an animation sequence of the  $2.4^\circ$  radial velocity imagery revealed that smaller outbound ve-

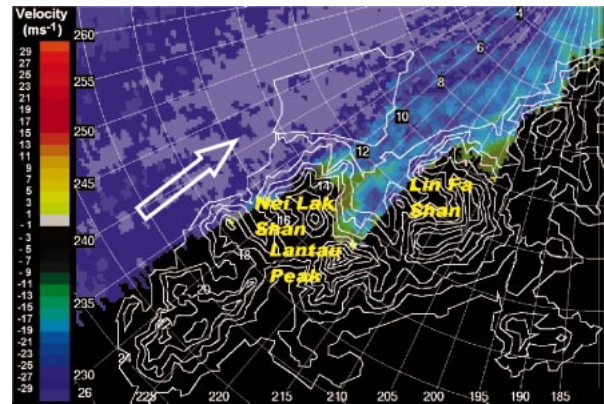


FIG. 5. TDWR radial velocity display at  $1.0^\circ$  elevation at 1408 UTC 2 Aug 1997. Tiny areas of outbound radial velocities can also be seen just downwind of Nei Lak Shan and Lantau Peak. White arrow indicates background flow direction.

locity bubbles were occasionally shed downwind of Lantau Peak and Lin Fa Shan and propagated downstream in the flow direction. One such outbound velocity bubble can be seen downstream of Lantau Peak in Fig. 6. As they propagated, these smaller outbound velocity bubbles quickly lost their outbound velocities but remained as part of the low-speed streaks emanating from the peaks. Sometimes they could be traced as individual low-speed bubbles while propagating downstream, especially when they were still close to the peaks. However, more often they became rather difficult to trace further downstream.

#### b. Hovmöller diagrams of radial velocity at 12-km range

To illustrate the time-dependent characteristics of the low-speed streaks and bubbles, azimuth–time Hovmöller plots of radial velocity downwind of the U-shaped ridge at 12-km radar range were constructed for the 1-h period between 1400 and 1500 UTC for elevation angles at  $0.6^\circ$ ,  $1.0^\circ$ , and  $2.4^\circ$  (Fig. 7).

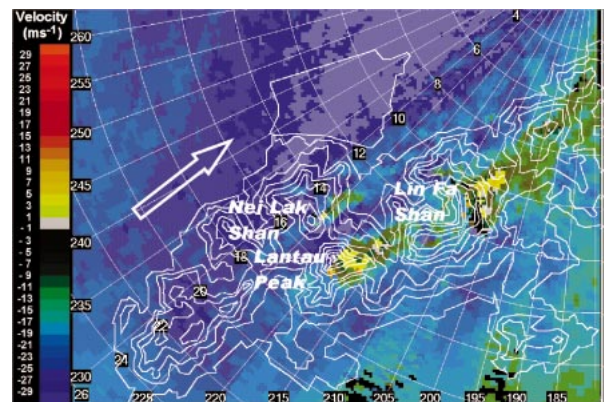


FIG. 6. TDWR radial velocity display at  $2.4^\circ$  elevation at 1407 UTC 2 Aug 1997. White arrow indicates background flow direction.

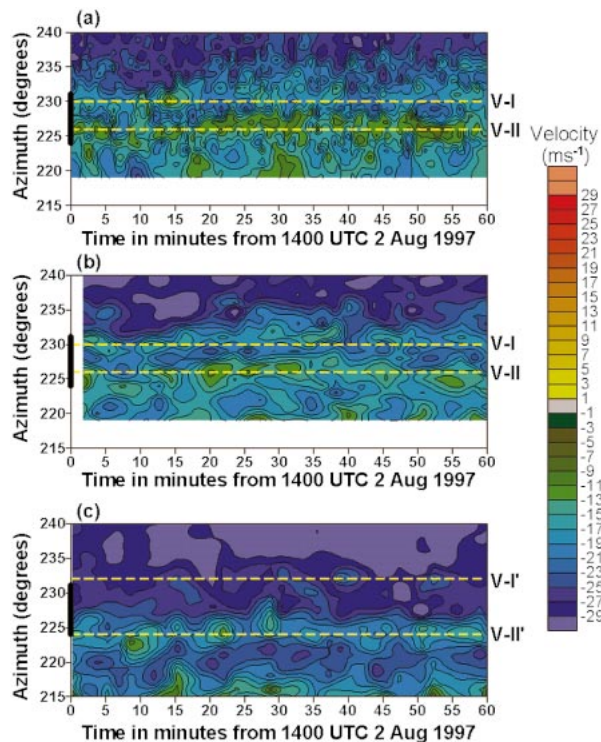


FIG. 7. Hovmöller diagram of TDWR radial velocity at 12-km radar range during 1400–1500 UTC 2 Aug 1997 at elevation angles of (a)  $0.6^\circ$ , (b)  $1.0^\circ$ , and (c)  $2.4^\circ$ . The black stripe on the azimuth axis marks the azimuthal position of the Nei Lak Shan terrain with heights above 500 m MSL.

At  $0.6^\circ$  elevation, the radar beam was located at a height of about 194 m MSL at 12-km radar range, lower than the mountain cols of the U-shaped ridge. Two low-speed streaks (i.e., in green on the velocity color scale) are immediately evident from Fig. 7a—one at an azimuth angle of about  $230^\circ$  (streak V-I) and the other at an azimuth angle of about  $226^\circ$  (streak V-II). Considering the mean azimuthal positions of these streaks, the background southwesterly flow, and the height of the radar beam relative to the terrain, it is evident that they were generated by terrain features of Nei Lak Shan. These streaks can be seen to meander within about  $1^\circ$  of their mean azimuthal positions. Not only could bubbles of local velocity minima be identified within these low-speed streaks, bubbles of local velocity maxima (i.e., in blue on the velocity color scale) are also evident between these low-speed streaks. The low- and high-speed bubbles appear to be temporally separated from their predecessors/successors by roughly 3–8 min, suggesting that they might be a result of periodic vortex shedding from the terrain features of Nei Lak Shan. Significant shear between adjacent high-speed and low-speed bubbles is also evident; for example,  $\approx 10 \text{ m s}^{-1}$  shear over  $1^\circ$  azimuth between 1420 and 1425, and between 1450 and 1455 UTC.

Let us turn to Fig. 7b, showing the Hovmöller dia-

gram of  $1.0^\circ$  elevation scans, also at 12-km radar range. The radar beam was located at a height of about 278 m MSL, still lower than the mountain cols of the U-shaped ridge. It is possible to identify streaks V-I and V-II in the same general azimuthal positions as in Fig. 7a. The low- and high-speed bubbles here appear to be temporally separated from their predecessors/successors by roughly 5–8 min. The lack of higher-frequency variations as compared with Fig. 7a may be explained by considering the longer time intervals (130 s on average) between the  $1.0^\circ$  elevation scans as compared with those between the  $0.6^\circ$  elevation scans (52 s on average).

Let us now look at Fig. 7c. At  $2.4^\circ$  elevation, the radar beam was located at a height of about 571 m MSL at 12-km radar range. Although this altitude is still lower than the peaks of Nei Lak Shan and Lantau Peak, it is already higher than the mountain col between the two peaks. In contrast with Figs. 7a and 7b, only one streak of low-speed bubbles can be identified in Fig. 7c at an azimuthal angle of about  $224^\circ$  (streak V-II') although one could argue that an additional low-speed streak might be present near  $232^\circ$  (streak V-I'). Following the discussions above, they were likely to be generated from the terrain features of Nei Lak Shan and might be correlated with streaks V-II and V-I identified at the lower elevations. However, their azimuthal positions differ from those of streaks V-I and V-II by a couple of degrees, suggesting that some vertical shear in the local wind field might be present. The periodicity of the low-speed bubbles within streak V-II' is clearly evident, with each bubble temporally separated from their predecessors/successors by roughly 5–8 min.

### c. Hovmöller diagrams of radial velocity along the $225^\circ$ azimuth

To further examine the temporal behavior of the streaks discussed above, range–time Hovmöller plots of radial velocity along the  $225^\circ$  azimuth were constructed for the same 1-h period for elevation angles at  $0.6^\circ$ ,  $1.0^\circ$ , and  $2.4^\circ$  (Fig. 8). This azimuth is chosen to illustrate the temporal variations at different distances downwind of Nei Lak Shan. In interpreting these diagrams, one should bear in mind that this azimuth is not exactly aligned with the background wind direction, and that at any given elevation angle, the radar beam was at different heights at different radar ranges.

Figure 8a shows the Hovmöller diagram for  $0.6^\circ$  elevation. The periodic appearance of the low-speed bubbles and the propagation of these low-speed bubbles toward the radar in the background southwesterly wind direction are clear. The average propagation speed (along the  $225^\circ$  azimuth) of these bubbles is estimated to be around  $15 \text{ m s}^{-1}$ . The frequency of the appearance and subsequent downstream propagation of the low-speed bubbles is on the order of 5–10 min. The amplitude of the temporal wind variations at a given radar range apparently decreased with increasing distance

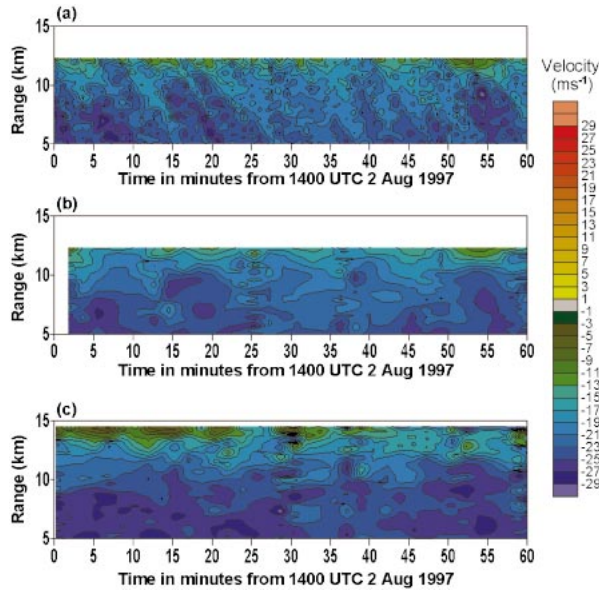


FIG. 8. Hovmöller diagram of TDWR radial velocity along 225° azimuth during 1400–1500 UTC 2 Aug 1997 at elevation angles of (a) 0.6°, (b) 1.0°, and (c) 2.4°.

downwind of Nei Lak Shan. This corroborates the earlier observation that the low-speed bubbles became rather difficult to trace farther downstream from their generation location.

Figures 8b and 8c show the Hovmöller diagrams for 1.0° and 2.4° elevations, respectively. Although there

are similarities when comparing Figs. 8b and 8c with Fig. 8a, the patterns in Figs. 8b and 8c are less clear, especially at short radar ranges. This is partly due to the lower temporal resolution of these higher-elevation data and partly due to the streaks at these higher elevations deviating from the 225° azimuth (cf. Figs. 4a, 5, and 6).

*d. Hovmöller diagrams of vertical profile of radial velocity*

As pointed out in section 3b above, Fig. 7c indicates periodic appearance of low-speed bubbles around 224° azimuth at 2.4° elevation at 12-km radar range. It would, therefore, be of some interest to consider the vertical structure of these low-speed bubbles.

Figure 9a shows a height–time Hovmöller plot of vertical profile of radial velocity constructed from the different elevation scans at 12-km radar range and 224° azimuth between 1400 and 1500 UTC. The location is at about 3.0 km downwind of Nei Lak Shan. Below the height of Nei Lak Shan (751 m MSL), not only is the periodic appearance of low-speed bubbles evident, the vertical alignment of these low-speed bubbles is also good along the lowest 500 m. A band of high radial velocity (up to about  $-25 \text{ m s}^{-1}$ ) is evident above 1000 m MSL. This band of high radial velocity is observed to penetrate to lower altitudes periodically, in between the low-speed bubbles. This was probably a result of descending flow across the col ( $\approx 460 \text{ m MSL}$ ) between

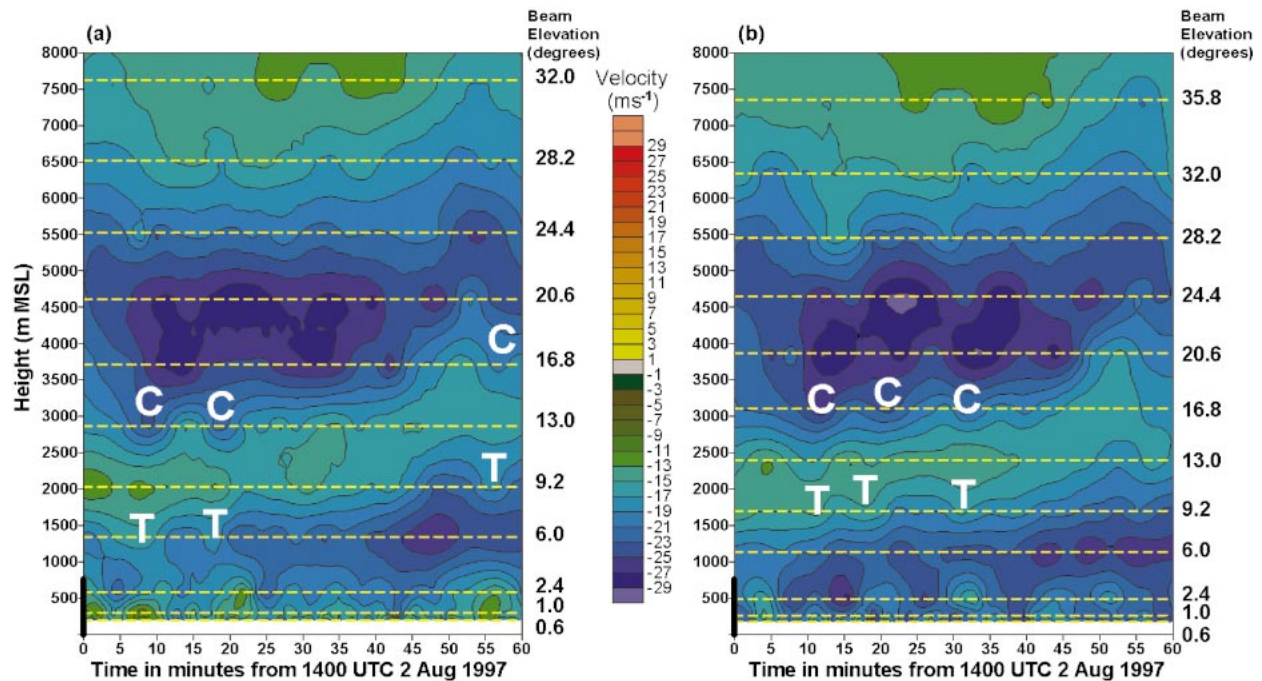


FIG. 9. Hovmöller diagram of vertical profile of TDWR radial velocity during 1400–1500 UTC 2 Aug 1997 at (a) 12-km radar range and 224° azimuth and (b) 10-km radar range and 224° azimuth. Altitudes of the radar beam at different elevation angles are marked on right-hand side for reference. Black stripe on the height axis marks the height of Nei Lak Shan.

Nei Lak Shan and Lantau Peak. Characteristics of flow across cols of the Lantau terrain will be further discussed in section 4 under the case of Typhoon Maggie.

Another interesting feature is the appearance of radial velocity “troughs” between 1000 and 1500 m MSL at around 1408 and 1418 UTC (marked as “T” in Fig. 9a). In view of the presence of a band of lower radial velocity between 1500 and 2500 m MSL, which was a larger-scale feature also observed by a wind profiler at Sham Shui Po about 25 km east of HKIA, these velocity troughs were likely to be caused by downward penetration of the band of lower radial velocity aloft. At about the same time when these troughs appeared, “crests” of high radial velocity were also observed between 2500 and 3000 m MSL (marked as “C” in Fig. 9a). These crests were likely to be caused by downward penetration of high radial velocity from above 3000 m MSL. Considering that the vertical profile was located immediately downwind of the Lantau terrain and no significant terrain was present upwind of Lantau, these troughs and crests are indicative of vertically propagating gravity waves excited by the Lantau terrain. A signature of gravity waves was also observed only at azimuths downwind of the Lantau terrain in the Hovmöller diagram of TDWR radial velocity at 12 km at  $6.0^\circ$  elevation (not shown).

Similar to Fig. 9a, Fig. 9b shows the time evolution of vertical profile of radial velocity at 10-km radar range at the same azimuth ( $224^\circ$ ), about 5.0 km downwind of Nei Lak Shan. Here the radial velocity below the height of Nei Lak Shan appears generally higher when compared with Fig. 9a. A periodic appearance of low-speed bubbles is still apparent, but these bubbles appear to be reduced in their vertical extent and have higher radial velocity when compared with those in Fig. 9a. This indicates that the low-speed bubbles weakened with increasing distance downstream of their generation location. It is also possible to identify signatures of gravity waves in Fig. 9b, at around 1410, 1418, and 1430 UTC.

#### e. Understanding of the observed phenomenon— Vortex shedding

The above analyses of TDWR data suggest that the observed low-speed streaks and bubbles were formed by vortex shedding downstream of the individual peaks of the U-shaped ridge of Lantau Island. This is strongly supported by (i) the reverse flows with outbound velocities observed on the immediate lee slopes of these peaks at  $2.4^\circ$  elevation, and (ii) the occasional shedding of these outbound velocities downstream. These reverse flows coupled with the high-speed flows on either side of the peaks indicate the presence of recirculation vortices. The lateral sizes of these recirculation vortices were estimated to be around 1–2 km. Furthermore, the reverse flows on the lee slopes of Lantau Peak and Nei Lak Shan observed at  $2.4^\circ$  (at around 700 m MSL) were also sometimes observed at  $1.0^\circ$  (at around 350 m MSL).

This suggests that the recirculation vortices were probably formed above 350 m MSL—roughly the level of the cols between Nei Lak Shan, Lantau Peak, and Sunset Peak. These recirculation vortices were apparently sources of significant shear vorticity. This was evidenced by the lateral shear resulting from some  $30 \text{ m s}^{-1}$  inbound high-speed flows and  $3\text{--}8 \text{ m s}^{-1}$  in the reverse flows, separated merely by a distance of 2 km or less.

While the shed vortices quickly lost their outbound velocities as they propagated downstream, they remained in the form of low-speed streaks/bubbles that still possessed shear vorticity of significant magnitude. Although there was some vertical tilting of the streaks as revealed by Fig. 7 (cf. streak V-II with streak V-II'), the low-speed bubbles have good vertical coherency in the lowest 500 m or so, as evident from Fig. 9a. This indicates that the shed vortices remained quasi two-dimensional at short distances downstream from their generation location.

From the identified range of frequencies of appearance of the low-speed bubbles in section 3b, we take the vortex-shedding frequency ( $\omega_s$ ) to correspond to the mean of the observed periods of 5–8 min, and obtain  $\omega_s = (6.5 \text{ min})^{-1} \approx 0.0026 \text{ Hz}$ . According to Atkinson (1981), the Strouhal number (St) for von Kármán vortex shedding downstream of islands is given by  $St = D\omega_s/U_0$ , where  $D$  is the island diameter, and St was observed to range between 0.15 and 0.32. For the present case, the low-speed bubbles were predominantly shed from NLS, which has a diameter of around 2 km at a height of 500 m MSL. From wind profiler data (not shown) at Sham Shui Po, about 2 km north of King's Park, winds strengthened during the period 1400–1500 UTC, and near the NLS terrain top height (751 m MSL), the wind was around  $234^\circ$  at  $29 \text{ m s}^{-1}$ . During the same 1-h period at station CCH over Cheung Chau (see Fig. 1 for location), a small island to the southeast of Lantau, the mean surface wind was  $229^\circ/22 \text{ m s}^{-1}$ . Taking  $D \approx 2 \text{ km}$  and  $U_0 \approx 25 \text{ m s}^{-1}$ , we obtain  $St_{\text{NLS}} \approx 0.21$ , which falls within the observed range noted above.

However, despite the agreement in the Strouhal number calculation, we are unable to find further evidence that the vortices shed were von Kármán vortices. We are unable to observe the characteristic sequence of shed vortices with alternating signs of rotation from the azimuthal shear pattern (Fig. 10) derived from the Hovmöller diagram in Fig. 7c. Furthermore, if we compute  $Nh/U_0$  for NLS, taking  $h = 751 \text{ m}$ ,  $N \approx 0.012 \text{ rad s}^{-1}$ , and  $U_0 \approx 25 \text{ m s}^{-1}$ , we obtain  $(Nh/U_0)_{\text{NLS}} \approx 0.36$ . This value falls outside the typical range for two-dimensional vortex shedding. We note that for  $Nh/U_0 \approx 0.36$  and Reynolds number ( $Re$ )  $\gg 10^3$ , the flow-regime diagram of Lin et al. (1992), based on a towing-tank study of stratified flow past a sphere with radius  $h$ , suggested that the flow regime fell into either “nonsymmetric vortex shedding” or “turbulent wake.” Although the results of Lin et al. (1992) may not be fully applicable in

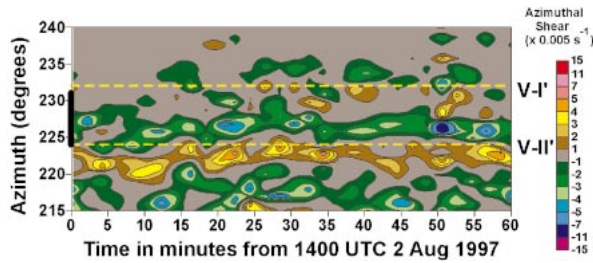


FIG. 10. Hovmöller diagram of azimuthal shear derived from the TDWR radial velocity data shown in Fig. 7c. The black stripe on the azimuth axis marks the azimuthal position of the Nei Lak Shan terrain with heights above 500 m MSL.

our case where  $Re = U_0 h / \nu \sim 10^9$  taking the kinematic viscosity  $\nu \approx 1.46 \times 10^{-5} \text{ m}^2 \text{ s}^{-1}$  for air at standard atmospheric sea level [Stull (1988), section 2.9.3], Baines (1995) suggested that towing tank results based on  $Re \gg 10^3$  should be adequate for studying atmospheric flow over complex terrain. With this, it may, therefore, be concluded that we observed vortex shedding either in the nonsymmetric vortex shedding regime or in the turbulent wake regime, although we are unable to determine exactly which of them is applicable to our case.

In discussing a study on stably and neutrally stratified flow over a model three-dimensional hill by Hunt and Snyder (1980), Baines (1995) noted that under the regime  $Nh/U_0 = 0.59$ , flow separation with reverse flow was expected downwind of the hill with the separated vortical wake region trailing downstream in a horseshoe pattern. At the same time, descending motion on the lee side due to stratification was also expected as part of a long-length-scale lee-wave pattern downwind of the hill. This descending motion would reduce and compress the separated wake region. All these results are consistent with the TDWR observations described earlier if we consider the observed vortex shedding as a time-dependent variation of the horseshoe vortical structure.

Vortex shedding in the wake of islands is a phenomenon well known from cloud patterns observed by meteorological satellites (Atkinson 1981). Numerical and field studies of stably stratified flow across islands and isolated obstacles have provided insights to the mechanisms of their formation (Nickerson and Dias 1981; Schär and Smith 1993a,b; Smith et al. 1997; Schär and Durran 1997). There are also recent observational and numerical studies of the so-called potential vorticity (PV) banners on the lee of the complex terrain of the Alpine region (Nance et al. 2000; Schär et al. 2003). However, we are not aware of any observational studies of wake flow in complex terrain that reveal such a high degree of details with results similar to the present case characterized by  $Nh/U_0 < 1$ .

#### 4. Typhoon Maggie—Terrain-induced vortices and high-speed flow

In contrast with Typhoon Victor, Maggie brought strong southerly flow to Lantau on 7–8 June 1999. The

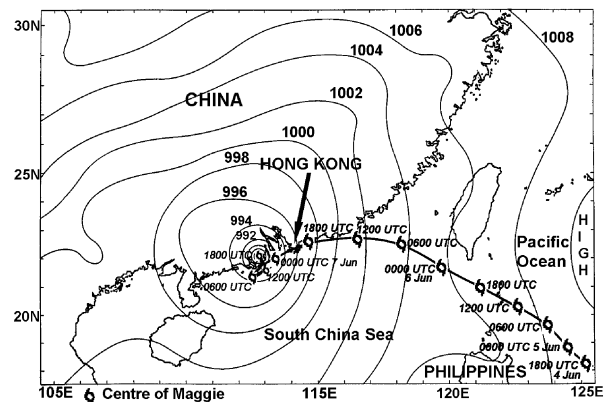


FIG. 11. Surface synoptic pressure chart at 1800 UTC 7 Jun 1999 with the track of Maggie overlaid.

complex terrain of Lantau projected a different cross section relative to the southerly flow direction and induced distorted flows with characteristics not displayed in the Victor case.

In the early morning of 7 June 1999, Typhoon Maggie, with estimated maximum winds of  $33 \text{ m s}^{-1}$ , made landfall over the northeastern part of Hong Kong and moved southwest rapidly. After departing Hong Kong, it slowed down and made a loop. It also weakened into a tropical storm with estimated maximum winds of  $23 \text{ m s}^{-1}$ . After the loop, Maggie moved northward in the evening and the winds in Hong Kong started to strengthen again from the south. Figure 11 shows the surface pressure chart at 1800 UTC with the track of Maggie overlaid. At HKIA, 1-min mean wind speeds reaching  $18 \text{ m s}^{-1}$  and 1-min gusts reaching  $27 \text{ m s}^{-1}$  were recorded. Winds at stations YTS and NLS (see Fig. 1 for locations) were even stronger, with 1-min mean speeds reaching  $34 \text{ m s}^{-1}$  at YTS and 1-min gusts reaching  $39 \text{ m s}^{-1}$  at NLS.

Figure 12 shows the wind and temperature profiles from radiosonde ascents launched at 1200 UTC 7 June 1999 and 0000 UTC 8 June 1999 at King's Park. During this period, apart from the lowest 500 m over which the wind flow might have been affected by hills to the south of King's Park, low-level winds remained southerly but strengthened as Maggie tracked northward. At 0000 UTC, wind speeds generally increased with height from about  $15 \text{ m s}^{-1}$  at 500 m MSL to almost  $25 \text{ m s}^{-1}$  at 1500 m. The average  $N$  is estimated to be about  $0.012 \text{ rad s}^{-1}$  between 500 and 1500 m MSL. During the night of 7 June 1999 and early morning of 8 June 1999, a number of aircraft reported wind shear and/or turbulence, mostly on approach to the airport from the west. From those flights that provided details of the events, wind shear with magnitude ranging from  $15 (7.7 \text{ m s}^{-1})$  to above  $25 \text{ kt} (12.9 \text{ m s}^{-1})$  and moderate turbulence were reported. Three of the flights also had their onboard wind shear warning system triggered. A total of six arrival flights had to conduct missed approaches because

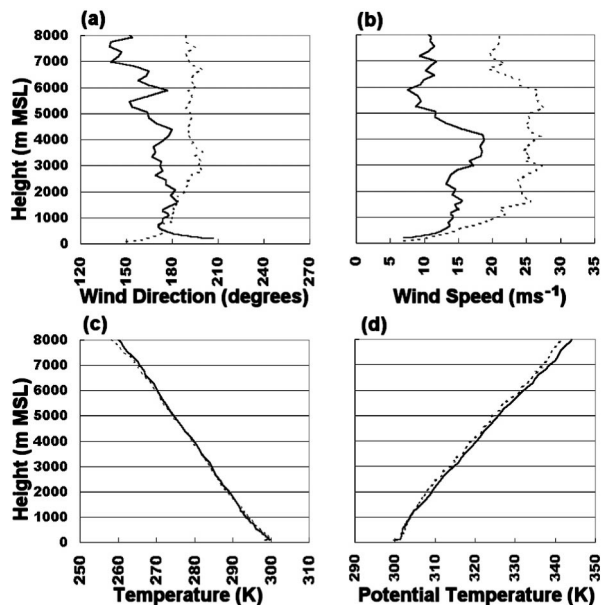


FIG. 12. King's Park radiosonde ascent at 1200 UTC 7 Jun 1999 (solid lines) and 0000 UTC 8 Jun 1999 (dotted lines): (a) wind direction ( $^{\circ}$ ), (b) wind speed ( $\text{m s}^{-1}$ ), (c) temperature (K), and (d) potential temperature (K).

of the wind shear and turbulence conditions, and two finally diverted to neighboring airports following abortive approaches.

*a. Radial velocity data of azimuthal scans*

Figures 13a and 13b show the  $0.6^{\circ}$  elevation radial velocity and reflectivity data at 1850 UTC 7 June 1999. In addition to the numerous north-northeast–south-southwest-oriented streaks of high- and low-speed inbound radial velocities, it is possible to identify in Fig. 13a two small-scale anticyclonic vortices with Doppler signatures of large inbound radial velocities, coupled with small outbound radial velocities. One was located to the southeast of the airport (vortex A), and the other one to the southwest of the airport (vortex B). The magnitudes of the inbound (and outbound) radial velocities associated with A and B were, respectively,  $-22$  ( $+4$ ) and  $-16$  ( $+2$ )  $\text{m s}^{-1}$ . While it was difficult to trace vortex B in the subsequent radar images because of inadequate radar return in low reflectivity, vortex A remained discernible in each of the subsequent radar images until 1855 UTC (Fig. 14). Figure 15 shows the positions of vortices A and B as observed on the  $0.6^{\circ}$  elevation data during the 5-min period. The speed of the northeasterly movement of vortex A was about  $15$ – $20$   $\text{m s}^{-1}$ . Although the small outbound radial velocity of the vortex signature for vortex A could no longer be observed after its first appearance at 1850 UTC, the large inbound radial velocities associated with vortex A could be seen throughout the period with smaller inbound radial velocities to its immediate southeast. Be-

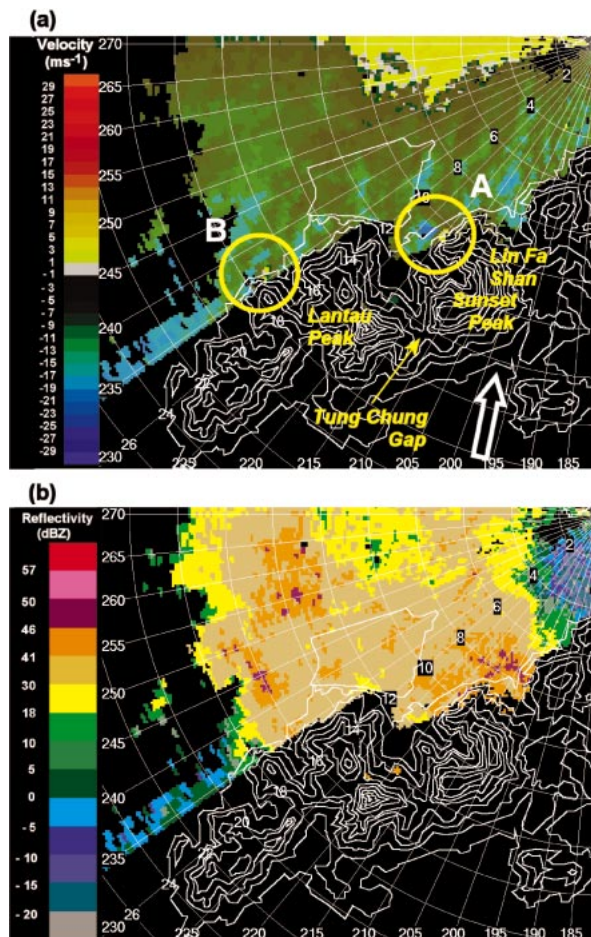


FIG. 13. (a) TDWR radial velocity display and (b) TDWR reflectivity display at  $0.6^{\circ}$  elevation at 1850 UTC 7 Jun 1999 with positions of vortices A and B marked. White arrow in (a) indicates background flow direction.

cause a size of only about 1 km across was involved, it is apparent that vortex A was associated with very large shear vorticity. Examination of data at  $1.0^{\circ}$  elevation during the same period (not shown) revealed that the size, strength, and location of vortex A resembled those observed at  $0.6^{\circ}$ . This indicates that, in the lowest 200 m or so, vortex A had a vertically aligned structure.

It is interesting to note in Fig. 14a, taken only several minutes after Fig. 13a, that three prominent high-speed streaks with lateral widths of about 2 km had formed—one over the airport (M-I), one to the northeast of Lin Fa Shan (M-II), and one upstream of vortex A in the middle of M-I and M-II (M-III). The inbound radial velocities of these high-speed streaks were generally around  $20$   $\text{m s}^{-1}$ , with maximums reaching  $24$ – $26$   $\text{m s}^{-1}$ . In contrast, the inbound radial velocities of the low-speed streaks between these high-speed streaks were only a few meters per second. Apparently, each of these high-speed streaks coupled with an adjacent low-speed streak to its west (east) would lead to large divergent (convergent) shear. In other words, each of these high-

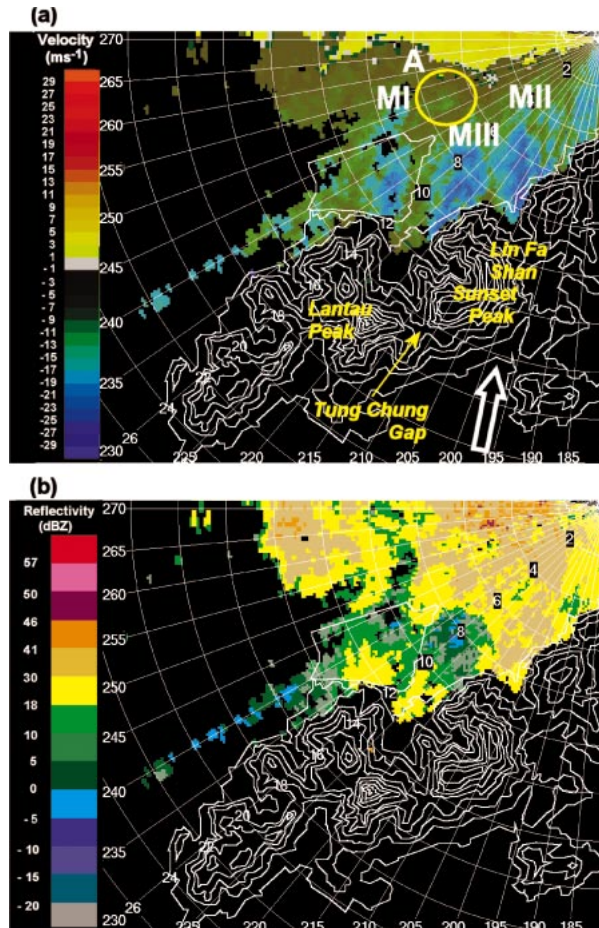


FIG. 14. (a) TDWR radial velocity display and (b) TDWR reflectivity display at  $0.6^\circ$  elevation at 1855 UTC 7 Jun 1999 with positions of vortex A and high-speed streaks M-I, M-II, and M-III marked. White arrow in (a) indicates background flow direction.

speed streaks was bounded by two shear lines—a convergent shear line to its east and a divergent shear line to its west. Indeed, the TDWR started to issue wind shear alerts at 1853 UTC as soon as these shear lines formed.

Examination of data at  $1.0^\circ$  (not shown) and  $2.4^\circ$  (Fig. 16) elevations revealed that the locations and strengths of these streaks were generally consistent with those observed at  $0.6^\circ$ . This indicates that these streaks were more or less vertically aligned in the lowest few hundred meters. Furthermore, comparing Fig. 16 with Fig. 14a shows that (i) streak M-III was associated with high-speed flow across Tung Chung Gap, (ii) streak M-I was associated with flow around the western side of Lantau Peak, and (iii) streak M-II was associated with flow around the eastern side of Lin Fa Shan. Figure 16 also reveals an extensive area of outbound radial velocity immediately downwind of Lantau Peak, connecting to the low-speed streak between M-I and M-III. Another low-speed streak with small areas of outbound radial velocity can also be identified between M-II and M-III

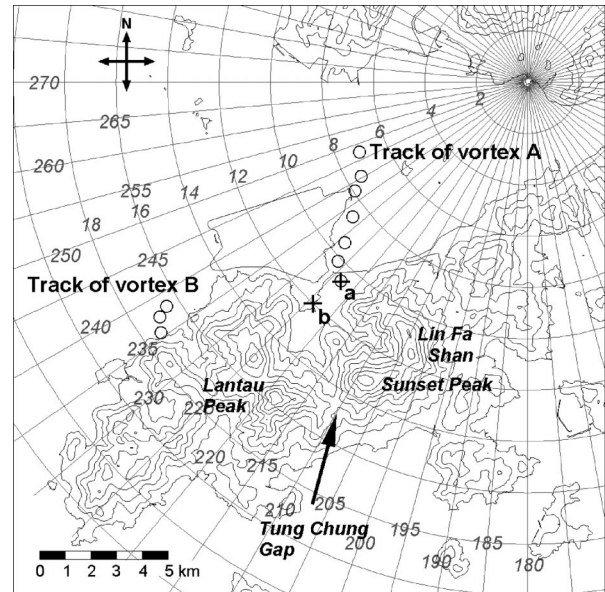


FIG. 15. Positions of vortices A and B as observed on the TDWR radial velocity display at  $0.6^\circ$  elevation between 1850 and 1855 UTC 7 Jun 1999. Locations of points a and b referred to in section 4c are also marked.

downwind of Sunset Peak and Lin Fa Shan. These features strongly resemble the vortex-shedding phenomena described in section 3 for the Victor case, with recirculation vortices on the immediate lee slope of the peaks of Lantau and high- and low-speed streaks emanating from the mountain cols and peaks respectively.

#### b. Hovmöller diagrams of radial velocity along $224^\circ$ azimuth

To examine the temporal behavior of streaks M-II and M-III discussed above, range–time Hovmöller plots of radial velocity along a fixed azimuthal angle of  $224^\circ$  were constructed for the period between 1830 and 1915 UTC for elevation angles at  $0.6^\circ$  and  $2.4^\circ$  (Fig. 17).

Figure 17a shows the Hovmöller diagram for  $0.6^\circ$  elevation. Within the 12-km radar range, the radar beam at  $0.6^\circ$  elevation was located below 200 m MSL—at least 150 m lower than the mountain cols of the U-shaped ridge. The most striking feature is the large increase of inbound radial velocity, associated with the high-speed streak M-III between the 7- and 10-km radar range, to more than  $25 \text{ m s}^{-1}$  just a few minutes after 1853 UTC. Because streak M-III is believed to be associated with high-speed flow across the Tung Chung Gap ( $\approx 340 \text{ m MSL}$ ) and the radar beam at  $0.6^\circ$  elevation was located at a height of just 136 m MSL at 7-km radar range, the high-speed flow must have descended by around 200 m to reach the lower levels. In saying this, we have taken into consideration the finite size of the radar beam, which has a cross-sectional diameter of

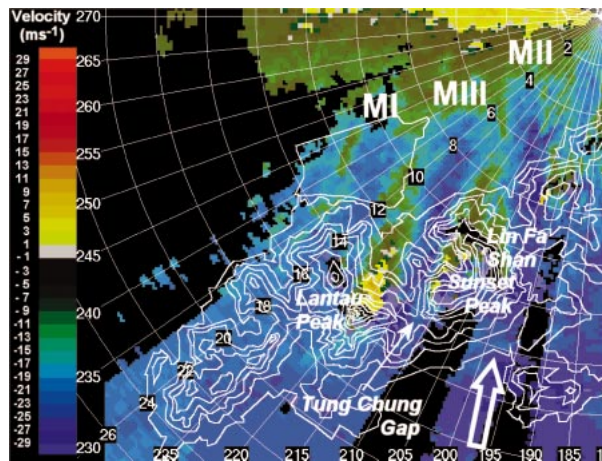


FIG. 16. Same as Fig. 14a, but for 2.4° elevation at 1856 UTC 7 Jun 1999.

67 m at 7-km radar range, considering the half-power beamwidth.

Figure 17a further indicates that the increase of inbound radial velocity associated with the high-speed streak M-II also appeared after 1853 UTC, spanning radar ranges from 2 to 6 km to the east of streak M-III. Although not appearing as strong as streak M-III, the high-speed flow associated with streak M-II exhibited similar temporal variations when compared with those of streak M-III, suggesting that these variations might be driven by a common mechanism.

The Hovmöller diagram for 2.4° elevation (Fig. 17b) also reveals similar features as in Fig. 17a, with the high-speed flow associated with streak M-III being most prominent after 1852 UTC (up to about  $-24 \text{ m s}^{-1}$  at around 1856 UTC). Here, it should be noted that at 2.4° elevation, the radar beam became just clear of the level of Tung Chung Gap at about 7-km radar range but was still below the peaks of the U-shaped ridge even up to 14-km radar range. In contrast with Fig. 17a, it is still possible to discern streak M-III almost continuously before 1852 UTC, albeit being weaker. Streak M-II was also observed to be rather persistent. At radar ranges between 12 and 14 km where the radar beam was located just downwind of Lantau Peak, low-speed flow with periodic speed variations, including the reverse flow at about 1910 UTC, is evident.

Before leaving Fig. 17b, some discussion on the apparent increase of about 30% of the maximum inbound radial velocity of streak M-III from about  $-18 \text{ m s}^{-1}$  before 1852 UTC to about  $-24 \text{ m s}^{-1}$  after 1852 UTC, as observed at 2.4° elevation, is appropriate. Upwind of Lantau Island, there was a change of the surface winds near 1844 UTC at CCH from around  $185^\circ$  to  $193^\circ$  together with an increase of the 1-min gusts from around 25 to  $28 \text{ m s}^{-1}$ . Resolving these winds along the 224° azimuth relative to the TDWR gives an inbound radial velocity of  $-19 \text{ m s}^{-1}$  before the change and  $-24 \text{ m s}^{-1}$  after the change. Although these values agree well

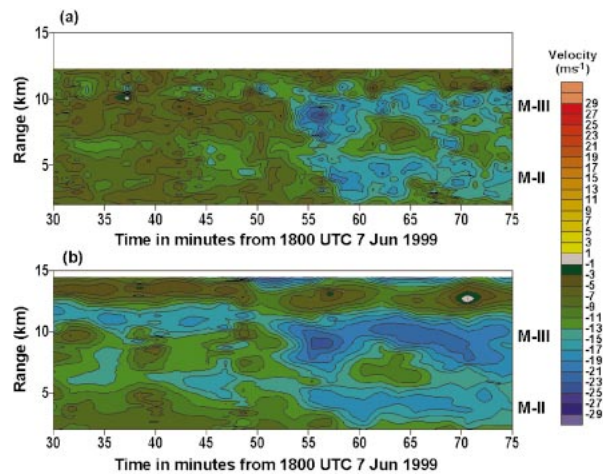


FIG. 17. Hovmöller diagram of TDWR radial velocity along 224° azimuth during 1830–1915 UTC 7 Jun 1999 at elevation angles of (a) 0.6° and (b) 2.4°.

the radar-observed values at the 2.4° elevation, the apparent “jump” of the maximum inbound radial velocity observed at 0.6° elevation from about  $-11 \text{ m s}^{-1}$  before 1850 UTC to beyond  $-25 \text{ m s}^{-1}$  a few minutes after 1853 UTC cannot be fully explained. Because this jump was apparently triggered by a relatively minor change of the upstream flow, the existence of a nonlinear mechanism with “threshold” behavior, such as the downslope wind mechanisms described in Durran (1990) or the gap flow mechanism described by Armi and Williams (1993), is suggested. Before considering further data to support this postulation, we examined the reflectivity fields in Figs. 13b and 14b, obtained from the same 0.6° scans that provided the velocity fields in Figs. 13a and 14a, to assess whether a surge of precipitation could have caused the jump in wind speed in the lower levels through an evaporatively cooled or rain-loaded downdraft. We note that at 1850 UTC when the high-speed streaks M-I, -II and -III had not yet appeared (Fig. 13a), an extensive area of precipitation with reflectivity up to 49 dBZ was present downwind of Lantau (Fig. 13b). As the high-speed streaks appeared (Fig. 14a), the main body of the precipitation area had moved farther north with M-I and M-III lying over a relatively low reflectivity area but with M-II still lying within a precipitation area with reflectivity up to 36 dBZ. It is, therefore, apparent that the precipitation had no direct relationship with the appearance of the high-speed streaks.

*c. Hovmöller diagrams of vertical profile of radial velocity*

Similar to the Victor case, we also constructed height–time Hovmöller plots of vertical profile of radial velocity to understand the vertical structure of the features described above. Because of data-quality problems, data above 13.0° elevation are not shown. Figure 18a shows

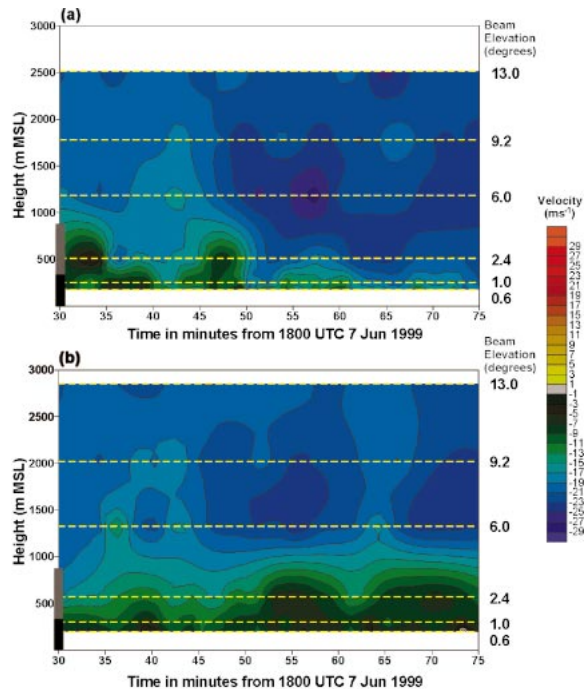


FIG. 18. Hovmöller diagram of vertical profile of TDWR radial velocity during 1830–1915 UTC 7 Jun 1999 at (a) 10.6-km radar range and  $223^\circ$  azimuth (point a) and (b) 12.0-km radar range and  $224^\circ$  azimuth (point b). See Fig. 15 for locations of points a and b. Manual editing was applied to remove suspicious velocity spikes. Black stripe (gray stripe) on the height axis marks the height of the Tung Chung Gap (Sunset Peak).

a Hovmöller diagram of vertical profile of radial velocity constructed from the available elevation scans at 10.6-km radar range and  $223^\circ$  azimuth between 1830 and 1915 UTC. This location (point a, see Fig. 15) was selected to capture the large inbound radial velocity associated with vortex A during its first appearance at 1850 UTC (Fig. 13a), and the subsequent emergence of the high-speed streak M-III (Fig. 14a). Point a is about 4.5 km downwind of Tung Chung Gap—the origin of streak M-III. The most striking feature revealed by Fig. 18a is the horn-shaped high-speed region that appeared after 1845 UTC. Before this time, low-speed bubbles with inbound radial velocity less than  $10 \text{ m s}^{-1}$  generally dominated altitudes below 1000 m MSL. However, at 1845 UTC the inbound radial velocity above 1500 m MSL started to increase from about 18 to over  $23 \text{ m s}^{-1}$  in only 5 min. This increase quickly extended to the lower altitudes with high-speed flow of around  $20 \text{ m s}^{-1}$  reaching the lowest 500 m MSL, reducing the vertical extent of the low-speed bubbles to only a few hundred meters. The high-speed core exceeding  $23 \text{ m s}^{-1}$  attained its lowest altitude at around 1905 UTC but then lifted again after 1910 UTC. At 1905 UTC, a local minimum of the inbound radial velocity (below  $20 \text{ m s}^{-1}$ ) can be identified between 1500 and 2000 m MSL but this appears too strong to be considered as a gap-flow stagnant area as described by Armi and Williams

(1993). Nevertheless, Fig. 18a indicates that there was an apparent descent of more than 1000 m of the high-speed flow aloft at about the same time that vortex A appeared in the lowest few hundred meters, followed shortly by the emergence of streak M-III in the lowest 200 m MSL that originated from Tung Chung Gap. These observations appear similar to the gap-flow phenomena observed over larger-scale terrain like the Brenner Pass of the Alps during the Mesoscale Alpine Programme (MAP) special observing period (Bougeault et al. 2001) even though the present case occurred in tropical cyclone conditions.

Figure 18b shows a Hovmöller diagram of vertical profile of radial velocity at 12.0-km radar range and  $224^\circ$  azimuth. This location (point b, see Fig. 15) represents a point within the low-speed streak between high-speed streaks M-I and M-III, about 3.5 km downwind of Lantau Peak. Similar to Fig. 18a, the inbound radial velocity around 1500 m MSL started to increase at 1845 UTC from about 18 to over  $23 \text{ m s}^{-1}$  in only 5 min. However, in strong contrast with Fig. 18a, the high-speed flow remained above 1000 m MSL without any apparent descent. Because the descent of high-speed flow observed in Fig. 18a only occurred downstream of the Tung Chung Gap, we conclude that the descent was a gap-related phenomenon. Before leaving Fig. 18b, we note that the two regions of increased inbound radial velocity above 1000 m MSL correspond well temporally with the two regions of decreased inbound radial velocity below 1000 m MSL, suggesting an increase in the wake circulation downwind of Lantau Peak simultaneous with the increase in flow speed aloft.

#### d. Understanding of the observed phenomenon—Gap-related downslope flow

From the above analyses of TDWR data, it is clear that the high-speed streak M-III observed in the lowest couple hundred meters originated from the Tung Chung Gap some 150–200 m above. This observation, together with evidence provided by the height–time Hovmöller plots of radial velocity, strongly suggests a descent of high-speed flow from aloft. Furthermore, the onset of this phenomenon was apparently preceded by a relatively insignificant change in the wind direction and speed of the upstream flow, suggesting the existence of a nonlinear mechanism with threshold behavior. Because such descent was not evident on the lee of Lantau Peak, we conclude that this phenomenon was gap related and, therefore, the gap flow mechanism described by Armi and Williams (1993) may be relevant here.

Apart from the threshold behavior of the gap-related downslope flow observed in the present case of Maggie, we recall from discussions in section 3d that periodic penetration of high-speed flow from aloft to lower altitudes was also observed downwind of the mountain col between Nei Lak Shan and Lantau Peak in the case of Victor. Section 3d also provides observational evi-

dence of the presence of vertically propagating gravity waves induced by the Lantau terrain. These indicate that, in addition to the gap flow mechanism, gravity wave dynamics may have an important role, and a discussion of the nondimensional mountain height  $Nh/U_0$  for the present case is in order here.

Taking  $N \approx 0.012 \text{ rad s}^{-1}$  and  $U_0 \approx 20 \text{ m s}^{-1}$ , we estimate that the nondimensional mountain height for LP was  $(Nh/U_0)_{LP} \approx 0.56$  with  $h = 934 \text{ m}$ . Here the determination of  $U_0 \approx 20 \text{ m s}^{-1}$  followed the methodology described in section 3e for the Victor case. During the period 1830–1915 UTC, the wind profiler at Sham Shui Po indicated winds of  $170^\circ/22 \text{ m s}^{-1}$  near the LP terrain-top height (934 m) and the mean surface wind at station CCH was  $190^\circ/20 \text{ m s}^{-1}$ . According to Hunt and Snyder (1980), in their study of stably and neutrally stratified flow over a model three-dimensional hill, apart from flow separation, reverse flow, and separated vortical wake region downwind of the hill, descending motion on the lee side due to stratification is also expected as part of a long-length-scale lee-wave pattern downwind of the hill under the regime  $Nh/U_0 = 0.59$ . However, we are unable to explain the threshold behavior of the descending high-speed flow observed in the present study.

Drobinski et al. (2001) presented a theoretical framework for diagnosing gap flow in the atmosphere based on the reduced-gravity shallow-water (RGSW) theory. In this theory, the fluid under consideration is bounded by a free surface, such as the presence of a low-level temperature inversion separating the boundary layer from the free atmosphere aloft. The RGSW theory, together with a single-layer shallow-water model, was also applied by Smith et al. (1997) to diagnose the wake of St. Vincent, including a gap-induced low-level jet, under the influence of stable stratification below the trade wind inversion. Noting that there was a sudden increase of stability associated with an isothermal layer between 1200–1300 m from the King's Park radiosonde ascent at 1200 UTC 7 June 1999 (Fig. 12d), the RGSW theory might be applicable in the present case. We estimate that the Froude number  $Fr = U_0/(g'H)^{1/2} \approx 2.8$  (taking  $U_0 \approx 20 \text{ m s}^{-1}$ ,  $H \approx 1250 \text{ m}$  as the depth of the stable layer, and  $g' = g\Delta\theta/\theta \approx 0.04 \text{ m s}^{-2}$  with  $\Delta\theta = 1.3 \text{ K}$  and  $\theta = 305.2 \text{ K}$  across the isothermal layer) and note that this Fr value was far from the critical value of 1 for hydraulic transition. It, therefore, appears that the formulation of the Froude number may need to be adjusted before the RGSW theory could be applied in the present case of deep uniform flow, especially within a tropical cyclone rainband.

## 5. Conclusions

In sections 3 and 4, we presented detailed TDWR observations of the complex three-dimensional wind flow in the lee of Lantau Island under different wind directions. The upstream flow speed and stability for

these two cases were similar with  $U_0 \approx 20\text{--}25 \text{ m s}^{-1}$ ,  $N \approx 0.012 \text{ rad s}^{-1}$ , and, thus, the flow conditions were characterized by  $Nh/U_0 < 1$  and  $Na/U_0 \sim O(1)$ , with  $h \sim O(1 \text{ km})$  and  $a \sim O(2 \text{ km})$ . The TDWR Doppler velocity datasets revealed features not previously observed by conventional instruments under similar weather conditions. Despite the complexity of the flow patterns, Hovmöller diagrams constructed from the Doppler velocity data brought out in considerable detail interesting patterns of temporal variations of the wind flow in the wake of Lantau Island. From these observations, we conclude that

- 1) high- and low-speed streaks with widths between a few hundred meters and a couple of kilometers were generated by the complex terrain of Lantau Island. Adjacent high- and low-speed streaks led to the formation of horizontal shear lines, which could bring significant wind shear to aircraft landing at or departing from HKIA;
- 2) the low-speed streaks consisted of low-speed bubbles resulting from vortices shed from the lee slopes of mountain peaks of Lantau Island. The Strouhal number of 0.21 derived for the quasi-two-dimensional vortex signatures at short distances downwind of the mountain peaks was consistent with documented observations for atmospheric von Kármán vortex streets; and
- 3) the descent of high-speed flow through mountain cols could be periodic as in the case of Victor, or could exhibit threshold behavior, as in the case of Maggie. Nonlinear dynamics such as gap flow and gravity wave mechanisms may be required to explain these phenomena.

We are not aware of any observational studies of wake flow over complex terrain that reveal such detail and have results similar to the present cases characterized by  $Nh/U_0 < 1$ . For numerical studies, while streaks of speed, vorticity, and vertical velocity streaming off the peaks of Lantau and propagating downstream were simulated by Clark et al. (1997) for a southeasterly deep uniform flow during the passage of Tropical Storm Russ, the presence of strong recirculation vortices on the immediate lee slopes, horizontal shear lines bringing significant wind shear to aircraft, and descending high-speed flow through mountain cols presented in this manuscript were not apparent in the simulation results. Also, Clark et al. (1997) concluded that mechanical effects rather than gravity wave dynamics were the dominating mechanism for the generation of TIWT downwind of Lantau. The observations presented in this manuscript, however, suggest that gap flow and gravity wave dynamics might have played an important role.

In situ reports by aircraft landing at or taking off from HKIA had confirmed that the flow variability in the lee of Lantau Island was capable of bringing wind shear in addition to turbulence of smaller scale. In view of the importance of these phenomena to the safe operation of

aircraft, there is a need to further understand their generation mechanisms and possible behavior, for instance by means of further numerical studies and/or physical modeling, bearing in mind that the roles of nonlinear gap flow and gravity wave dynamics cannot be neglected.

*Acknowledgments.* The authors thank the anonymous referees who helped to significantly improve the manuscript; Richard Doviak, Herbert Puempel, Ronald Smith, and B. Y. Lee for providing very useful comments on earlier versions of the manuscript; and Christoph Schär, Dusan Zrnić, and C. M. Cheng for fruitful discussions on interpretation of the radar data. We also thank the U.S. Federal Aviation Administration for making available the WxShell Software of the Lincoln Laboratory of the Massachusetts Institute of Technology for TDWR data visualization.

#### REFERENCES

- Armi, L., and R. Williams, 1993: The hydraulics of stratified fluid flowing through a contraction. *J. Fluid Mech.*, **251**, 355–375.
- Atkinson, B. W., 1981: *Meso-scale Atmospheric Circulations*. Academic Press, 495 pp.
- Baines, P. G., 1995: *Topographic Effects in Stratified Flows*. Cambridge University Press, 482 pp.
- Bougeault, P., and Coauthors, 2001: The MAP Special Observing Period. *Bull. Amer. Meteor. Soc.*, **82**, 433–462.
- Clark, T. L., T. Keller, J. Coen, P. Neilley, H. Hsu, and W. D. Hall, 1997: Terrain-induced turbulence over Lantau Island: 7 June 1994 Tropical Storm Russ case study. *J. Atmos. Sci.*, **54**, 1795–1814.
- Drobinski, P., J. Dusek, and C. Flamant, 2001: Diagnostics of hydraulic jump and gap flow in stratified flows over topography. *Bound.-Layer Meteor.*, **98**, 475–495.
- Durran, D. R., 1990: Mountain wave and downslope winds. *Atmospheric Processes over Complex Terrain, Meteor. Monogr.*, No. 45, Amer. Meteor. Soc., 59–81.
- Hunt, J. C., and W. H. Snyder, 1980: Experiments on stably and neutrally stratified flow over a model three-dimensional hill. *J. Fluid Mech.*, **96**, 671–704.
- Lin, Q., W. R. Lindberg, D. L. Boyer, and H. J. S. Fernando, 1992: Stratified flow past a sphere. *J. Fluid Mech.*, **240**, 315–354.
- Michelson, M., W. W. Shrader, and J. G. Wieler, 1990: Terminal Doppler Weather Radar. *Microwave J.*, **33**, 139–148.
- Nance, L. B., and Coauthors, 2000: Observations of potential vorticity banners during the Mesoscale Alpine Programme. Preprints, *Ninth Conf. on Mountain Meteorology*, Aspen, CO, Amer. Meteor. Soc., 43–48.
- Neilley, P. P., G. B. Foote, T. L. Clark, L. B. Cornman, H. Hsu, T. L. Keller, J. Tuttle, and A. R. Rodi, 1995: Observations of terrain-induced turbulent flow in the wake of a mountainous island. Preprints, *Seventh Conf. on Mountain Meteorology*, Breckenridge, CO, Amer. Meteor. Soc., 264–269.
- Nickerson, E. C., and M. A. Dias, 1981: On the existence of atmospheric vortices downwind of Hawaii during the HAMEC Project. *J. Appl. Meteor.*, **20**, 868–873.
- Schär, C., and R. B. Smith, 1993a: Shallow-water flow past isolated topography. Part I: Vorticity production and wake formation. *J. Atmos. Sci.*, **50**, 1373–1400.
- , and —, 1993b: Shallow-water flow past isolated topography. Part II: Transition to vortex shedding. *J. Atmos. Sci.*, **50**, 1401–1412.
- , and D. R. Durran, 1997: Vortex formation and vortex shedding in continuously stratified flows past isolated topography. *J. Atmos. Sci.*, **54**, 534–554.
- , M. Sprenger, D. Lüthi, Q. Jiang, R. B. Smith, and R. Benoit, 2003: Structure and dynamics of an Alpine potential-vorticity banner. *Quart. J. Roy. Meteor. Soc.*, **129**, 825–855.
- Shun, C. M., 2003: Ongoing research in Hong Kong has led to improved wind shear and turbulence alerts. *Int. Civil Aviation Org. J.*, **58**, 4–6, 28.
- Smith, R. B., A. C. Gleason, P. A. Gluhosky, and V. Grubišić, 1997: The wake of St. Vincent. *J. Atmos. Sci.*, **54**, 606–623.
- Stull, R. B., 1988: *An Introduction to Boundary Layer Meteorology*. Kluwer Academic, 666 pp.